Sustainable Energy & Fuels

ROYAL SOCIETY OF CHEMISTRY

PAPER

View Article Online
View Journal | View Issue

Cite this: *Sustainable Energy Fuels*, 2024, **8**, 2751

Sheet-like $ZnCo_2O_4$ microspheres and pomelo peel waste-derived activated carbon for high performance solid state asymmetric supercapacitors†

Kiran Kumar Reddy Reddygunta, [a] Lidija Šiller[b] and Aruna Ivaturi *[a]

A novel asymmetric supercapacitor based on zinc cobalt oxide ($ZnCo_2O_4$) as a positive electrode and pomelo peel-based activated carbon (PPAC-4) as a negative electrode was fabricated. $ZnCo_2O_4$ was synthesized using hydrothermal method and shows a distinct sheet-like structure clubbed together to form microspheres. PPAC-4 was synthesized *via* the chemical activation of pomelo peel hydrochar using $KHCO_3$ as the activation agent. The as-prepared $ZnCo_2O_4$ microspheres displayed maximum specific capacitance of 422 F g^{-1} at an applied current density of 1 A g^{-1}, whereas PPAC-4 demonstrated a capacitance of 356 F g^{-1} at a current density of 1 A g^{-1}. Moreover, the novel $ZnCo_2O_4$//PPAC-4 asymmetric solid-state supercapacitor with hydroxyethyl cellulose/potassium hydroxide (HEC/KOH) gel electrolyte displayed maximum operating voltage of 1.6 V with a superior energy density of 29.8 W h kg^{-1} at a power density of 796.3 W kg^{-1}. Besides, a long-term cycling stability of 83% was achieved after 10 000 charge/discharge cycles, indicating its promise for future energy storage applications.

Received 4th February 2024
Accepted 13th May 2024

DOI: 10.1039/d4se00182f

rsc.li/sustainable-energy

Introduction

Supercapacitors have drawn considerable interest because of their ability to instantly offer more power and energy densities that lie between those of traditional batteries and dielectric capacitors, along with prolonged lifespan.[1,2] Electric double-layer capacitors (EDLCs) and faradaic pseudocapacitors are further subcategories of supercapacitors based on their charge storing mechanism. EDLCs store charge *via* electrostatic adsorption/desorption of electrolyte ions at the electrode/electrolyte junction. Carbonaceous materials such as activated carbon, carbon nanotubes, and graphene are the preferred electroactive materials for EDLCs owing to their unique characteristics such as large specific surface area (SSA), superior electrical conductivity and good electrochemical stability. However, EDLCs deliver extremely low capacitance and energy densities, which impede their commercial applications. Conversely, a great deal of research has been conducted on pseudocapacitive materials as substitute electrode materials for supercapacitors to increase their energy densities. These materials include conducting polymers and transition metal derivatives with highly reversible redox reactions across the electrode/electrolyte interface. However, pseudocapacitive materials show some shortcomings such as low conductivity, limited power densities and poor cycling stability.[3,4] Coupling the positive effects of EDLCs and pseudocapacitive electrodes in a single unit results in an asymmetric supercapacitor, where charge storage takes place due to both electrostatic and redox reactions. As a result, fabricating an asymmetric supercapacitor that uses carbonaceous materials as negative electrodes and pseudocapacitive materials as positive electrodes yields a better voltage window, taking advantage of both the faradaic redox-type behavior and EDLCs significantly enhancing the energy density.[5,6]

On account of its exceptional structural and electrochemical characteristics, such as large SSA, interconnected porous architecture, high conductivity, and excellent electrochemical stability, biomass activated carbon (AC) is an ideal negative electrode material for constructing asymmetric supercapacitors.[7] Moreover, the production of activated carbon from biomass has various benefits, including the possibility for industrial scale production, renewability, abundance, and environmental friendliness. Several types of agricultural wastes have been utilized as renewable precursors for the production of porous carbons for use in supercapacitors.[8] Pomelo, a citrus fruit available in almost every corner of the world, is rich in nutrients and has high medicinal value. However, its peels are largely discarded as waste, though they can be used as a renewable source for synthesizing large surface area activated carbon. Numerous studies have been published on the use of

[a]*Smart Materials Research and Device Technology (SMaRDT) Group, Department of Pure and Applied Chemistry, University of Strathclyde, Thomas Graham Building, Glasgow, G1 1XL, UK. E-mail: aruna.ivaturi@strath.ac.uk*

[b]*School of Engineering, Newcastle University, Newcastle upon Tyne, NE1 7RU, UK*

† Electronic supplementary information (ESI) available: Additional figures related to XRD, BET, Raman and XPS. See DOI: https://doi.org/10.1039/d4se00182f

porous carbon materials derived from pomelo peel waste as electrodes in supercapacitors. For instance, Liang *et al.*[9] produced honeycomb like activated carbon (HLPC), which possessed a SSA of 2725 $m^2 g^{-1}$ and displayed a specific capacitance of 342 F g^{-1} at 0.2 A g^{-1}. Furthermore, in 6 M KOH electrolyte, the HLPC electrode-based symmetric supercapacitor exhibited an energy density of 9.4 W h kg^{-1}. Peng *et al.*[10] fabricated a symmetric supercapacitor with high SSA (2105 $m^2 g^{-1}$) pomelo peel-derived carbon electrodes and 1 M $NaNO_3$ aqueous electrolyte, which displayed an energy and power density of 17.1 W h kg^{-1} and 420 W kg^{-1}, respectively. In other instances, Wang *et al.*[11] fabricated dual-doped activated carbon from pomelo peels with nitrogen (N) and phosphorous (P), which exhibited an energy density of 11.7 W h kg^{-1} at 160 W h kg^{-1} when tested as a symmetric supercapacitor electrode in 1 M Na_2SO_4 aqueous electrolyte. Similarly, N,S-doped sponge-like activated carbon (NSC-600) was produced from pomelo peels, which showed a SSA of 1193 $m^2 g^{-1}$ and capacitance of 310 F g^{-1} at 0.5 A g^{-1} current density in 6 M KOH electrolyte. Moreover, the assembled symmetric supercapacitor with NCS-600 electrodes and PVA/H_2SO_4 electrolyte showed high energy and power density of 21.4 W h kg^{-1} and 2600 W kg^{-1}. However, the previously cited research demonstrated the fabrication of symmetric supercapacitors using porous carbon generated from pomelo peels waste and aqueous/synthetic polymer gel electrolytes. As far as we are aware, there is only one published work on the utilization of pomelo peel activated carbon as a negative electrode in an asymmetric supercapacitor. Qu *et al.*[12] synthesized N-doped carbon (PFNC) with high SSA (1648.6 $m^2 g^{-1}$), which displayed a specific capacitance of 260 F g^{-1} in 2 M KOH electrolyte at 1 A g^{-1}. Furthermore, the assembled asymmetric supercapacitor with porous nickel oxide (PFN)-based positive electrode and PFNC negative electrode displayed an energy density of 27.75 W h kg^{-1} at 300 W kg^{-1} power density in 2 M KOH electrolyte. Although the asymmetric supercapacitor discussed above showed excellent charge storage performance, the device was evaluated in an aqueous electrolyte system, which may not be suitable for practical application. Thus, in the present work, high SSA activated carbon has been produced from pomelo peel wastes and utilized as a negative electrode to prepare an asymmetric supercapacitor with HEC/KOH gel electrolyte.

Binary metal oxides such as cobalt molybdenum oxide ($CoMoO_4$),[13,14] copper cobalt oxide ($CuCo_2O_4$),[15,16] nickel cobalt oxide ($NiCo_2O_4$),[17,18] and zinc cobalt oxide ($ZnCo_2O_4$)[19,20] have been explored as novel pseudocapacitive electrodes in the past decade. These binary transition metal oxides are composed of one or more electrochemically active/inactive ions and at least one transition metal ion. Because binary metal oxides include multivalent oxidation states for several metal cations, they perform exceptionally well in terms of capacitance when compared to single metal oxide materials.[21,22] Among them, $ZnCo_2O_4$ has a maximum theoretical specific capacitance of 2604 F g^{-1} as well as multiple valence states that allow a variety of reversible redox reactions, which in turn leads to high energy storage performance. Rajesh *et al.*[20] prepared coral-like $ZnCo_2O_4$ nanostructures, which showed a specific capacity of 694 F g^{-1} at 2 A g^{-1} current density in 2 M KOH electrolyte. Chen *et al.*[19] also reported mesoporous $ZnCo_2O_4$ microspheres, which exhibited a specific capacitance of 689 F g^{-1} at 1 A g^{-1} current density. To the best of our knowledge, there have been very few studies on employing $ZnCo_2O_4$ as a positive electrode for asymmetric supercapacitors. Chen *et al.*[23] fabricated asymmetric supercapacitors utilizing activated carbon as the negative electrode and $ZnCo_2O_4$ quasi cubes as the positive electrode. The fabricated supercapacitor achieved an energy density of 34.4 W h kg^{-1} at a power density of 860.1 W kg^{-1} in 2 M KOH electrolyte and retained 79.2% of its capacitance after 3000 charge/discharge cycles at 5 A g^{-1}. Similarly, Zhu *et al.*[24] reported $ZnCo_2O_4$ and activated carbon-based asymmetric supercapacitor with excellent energy density of 36.31 W h kg^{-1} in 2 M KOH aqueous electrolyte. However, in both the above-mentioned cases, the asymmetric supercapacitors were fabricated with aqueous electrolyte, which poses severe safety constraints (volatile when exposed to high temperatures and leakage problems) and limits their practical application. Hence, in the present work, zinc cobalt oxide ($ZnCo_2O_4$) and pomelo peel-derived porous carbon were employed as the positive and negative electrode to fabricate an asymmetric supercapacitor that delivers high energy and power density. The microsphere-like $ZnCo_2O_4$ sheets were prepared through the hydrothermal process, and the activated carbon was prepared by the hydrothermal carbonization and $KHCO_3$ activation of pomelo peel waste. Pomelo peel-derived activated carbon and $ZnCo_2O_4$ electrodes were successfully integrated into an asymmetric supercapacitor device, which exhibits superior electrochemical properties in hydroxyethyl cellulose/potassium hydroxide (HEC/KOH) electrolyte with 1.6 V working voltage, superior energy density of 29.8 W h kg^{-1} at a power density of 796.3 W kg^{-1}, along with excellent cyclic stability (83%) after 10 000 chare/discharge cycles. The current study shows that the synergistic pairing of pomelo peel-derived porous carbon and $ZnCo_2O_4$ nanostructures has the potential to improve supercapacitor performance while also providing a sustainable approach of utilising pomelo peel waste for energy storage.

Experimental section

Materials and reagents

Pomelo fruit was bought from a nearby store in Edinburgh, UK and used as a carbon source. The following materials were purchased from Sigma-Aldrich: potassium hydroxide (KOH), potassium bicarbonate ($KHCO_3$, 99.7%), polyvinylidene fluoride (PVDF) binder, 1-methylpyrrolidone, hydroxyethyl cellulose (HEC), zinc nitrate hexahydrate [$Zn(NO_3)_2 \cdot 6H_2O$, 99%], cobalt nitrate hexahydrate [$Co(NO_3)_2 \cdot 6H_2O$, 98%], and urea [CH_4N_2O]. Hydrochloric acid (HCl, 37%) was procured from Fisher Scientific.

Synthesis of activated carbon from pomelo peels (PPAC-*N*)

For the preparation of activated carbon from pomelo peels, a pre-hydrothermal treatment followed by chemical activation was followed. 3 g of dried pomelo peel waste was cut into small

pieces and crushed into a powder, mixed with 40 mL of 1 M $KHCO_3$ solution, placed in a 120 mL autoclave, and heated to 180 °C for 24 h. After 24 h, the resultant product was rinsed with deionized (DI) water and annealed at 80 °C for 24 h to obtain hydrochar. In the next step, the obtained hydrochar was calcined at 850 °C for 2 h in a tube furnace, followed by washing with 1 M HCl and DI water until it reached a neutral pH. Finally, the obtained product after washing was dried overnight at 80 °C in a hot air oven. For comparison purposes, different $KHCO_3$ concentrations (1 M, 2 M, 3 M, 4 M, and 5 M) were also prepared using the above-mentioned procedure and the samples were termed as PPAC-*N*, where *N* specifies the $KHCO_3$ concentration. Owing to PPAC-4's better performance over other samples, extensive electrochemical investigations were conducted using the optimized PPAC-4.

Synthesis of zinc cobalt oxide ($ZnCo_2O_4$)

Typically, 0.1 M of $Zn(NO_3)_2 \cdot 6H_2O$ and 0.2 M of $Co(NO_3)_2 \cdot 6H_2O$ were mixed with 40 mL of DI water and stirred continuously for 60 min. After 60 min, urea was added to the above precursor solution, which was vigorously stirred for 2 h. The finished product was put into a stainless-steel autoclave and heated at 120 °C for 16 h. The pink coloured precipitate was then collected, washed with DI water several times and dried at 80 °C overnight. The resulting product was finally annealed at 350 °C for 2 h in a muffle furnace, and a black-coloured $ZnCo_2O_4$ powder was finally obtained for further characterization.[25]

Material characterization

The crystalline structure was recorded using X-ray diffraction (XRD, Bruker D2 Phaser system). Using a Micrometrics ASAP 2020 porosity analyzer operating at 77 K, the SSA and pore volume were examined using the Brunauer–Emmett–Teller (BET) and Non-Linear-Density-Functional-Theory (NLDFT) methods. The materials were degassed for 3 h at 300 °C in a dynamic vacuum before the SSA examinations. In order to investigate the defective/graphitic nature of the as-prepared samples, Raman spectra were obtained utilizing WiTec Raman microscope with 532 nm excitation wavelength within the 500 to 3500 cm^{-1} spectral range. A 10X objective lens was used with an acquisition duration of 10 s, and the laser power was adjusted to 14.7 mW. Samples were examined under a microscope, and five distinct spectra were taken from various sample sections. These spectra were then averaged using a MATLAB script to provide a representative spectrum. An FEI Quanta 250 FEGSEM employing 5 kV electron beam was used to obtain the surface morphology of the samples. An FEI Titan Themis operating at 200 kV, fitted with a CEOS DCOR probe corrector, a Super-X energy dispersive X-ray spectrometer (EDX), and a 4k × 4k Ceta CMOS camera, was used to perform high-angle annular dark-field canning transmission electron microscopy (HAADF-STEM) experiments. X-ray photoemission spectroscopy (XPS) investigation was carried out using a Thermo Scientific K-alpha X-ray Photoelectron Spectrometer™ (Thermo Scientific, East Grinstead, UK). Using a 0.05 eV energy step size, high resolution photoemission spectra of the required element areas were obtained at a 40 eV pass energy using a hemispherical electron analyzer. A monochromatic Al Kα X-ray source with a maximum X-ray beam spot size of 400 μm and an output energy of 1486.6 eV was used to acquire the spectra. Using a dual-beam electron/ion flood gun with low energy, surface charge correction was achieved. All XPS and Raman spectra were normalized, and using Fityk software, Voigt fitting was utilized to deconvolute the spectra.

Preparation of working electrodes and device for electrochemical measurements

PPAC-4 electrode was prepared by coating a homogenous slurry (consisting of 90 : 10 ratio of PPAC-4 and PVDF along with a few drops of 1-methylpyrrolidine) onto a 1 cm^2 area of the stainless-steel mesh (3 cm × 1 cm) and then dried at 80 °C for 2 h. $ZnCo_2O_4$ electrode was prepared by mixing pure $ZnCo_2O_4$, PPAC-4 and PVDF in a weight ratio of 80 : 10 : 10 mixed thoroughly with 1-methylpyrrolidone. The slurry was coated over 1 cm^2 area of stainless-steel mesh (3 cm × 1 cm) and then dried for 2 h at 80 °C. The stainless-steel mesh had a 0.026 mm aperture and a wire diameter of 0.025 mm.

For two electrode measurements, the $ZnCo_2O_4$//PPAC-4 asymmetric supercapacitor (Swagelok cell) was assembled with HEC/KOH gel electrolyte where $ZnCo_2O_4$ and PPAC-4 act as the positive and negative electrodes, respectively. The electrodes were prepared by coating the respective slurry (mentioned above) on circular (diameter = 1.4 cm) stainless-steel mesh current collectors. The bio-polymer (HEC/KOH) gel electrolyte was prepared by dissolving 2 g of HEC in 20 mL DI water, which was stirred continuously at 90 °C for 1 h. Later, 2 g of KOH, dissolved in 10 mL of DI water, was added dropwise to the HEC mixture for 15 min, and the resulting mixture was stirred further for 1 h at 90 °C. A transparent HEC/KOH gel electrolyte was obtained after 2 h, which was then placed inside a desiccator overnight to remove air bubbles in the gel and dried on the lab bench to obtain a white-coloured gel film. The circular electrodes were sandwiched together separated by the electrolyte film.

Electrochemical measurements

Through the use of electrochemical impedance spectroscopy (EIS), galvanostatic charge discharge (GCD), and cyclic voltammetry (CV), the charge storage ability of $ZnCo_2O_4$ and PPAC-4 electrodes were investigated. Using an Autolab PGSTAT 302N potentiostat/galvanostat with FRA32M module, all CV, GCD, and EIS experiments were performed at room temperature. Ag/AgCl, platinum wire, and active material coated stainless steel mesh were utilized as the reference, counter, and working electrodes, respectively, for a standard three-electrode experiment. The gravimetric specific capacitance (C_s) of the electrode was measured using GCD curves by means of eqn (1)[2,26]

$$C_s = \frac{I \times \Delta t}{m \Delta V} \quad (1)$$

where m is the mass of the active material on the electrode, Δt is the discharge time after IR drop, I is the current (in ampere), and ΔV is the potential window during the discharge process.

For a two-electrode device, the total capacitance C_t (F g^{-1}), energy density E_d (W h kg^{-1}) and power density P_d (W kg^{-1}) were measured from the GCD curves by means of eqn (2)–(5)[27,28]

$$C_t = \frac{I}{M\left(\frac{\Delta V}{\Delta t}\right)} \quad (2)$$

$$E_d = \frac{1}{2}\frac{C_t \times \Delta V^2}{3.6} \quad (3)$$

$$P_d = \frac{E_d \times 3600}{\Delta t} \quad (4)$$

where $(\Delta V/\Delta t)$ is the area under the discharge curve and M is the total weight of the active material in the two electrodes.

For the construction of an asymmetric supercapacitor, the charge balance will follow the relationship $q^+ = q^-$. The specific capacitance (C_s), potential range for the charge/discharge process (ΔV), and electrode mass (m) determine the amount of charge held by each electrode, as indicated in eqn (5).[29,30]

$$q = C_s \times \Delta V \times m \quad (5)$$

In order to get $q^+ = q^-$, the mass balancing will follow eqn (6).

$$m^+/m^- = C_{s-} \times \Delta V^-/C_{s+} \times V^+ \quad (6)$$

The mass ratio of $m(ZnCo_2O_4)/m$(PPAC-4) was estimated to be 1.46 from the specific capacitance calculated from their GCD curves.

Results and discussions

XRD studies

The crystalline phase and microstructure of the PPAC-*N* and $ZnCo_2O_4$ samples were studied using X-ray diffraction measurements. The XRD patterns of all PPAC-*N* materials were identical, as shown in Fig. 1(a) and S1(a),† with peaks at 2θ = 26.1° and 44.2° corresponding to the (002) and (100) planes, respectively, of amorphous carbon structures with partially graphitic nature.[2,31] The high intensity in the low angle region could potentially be attributed to the micropores found in PPAC-*N*.[32] A close analysis reveals the existence of a broad peak at 23°, which can be ascribed to the (100) plane of graphitic carbon found in amorphous carbon structures.[33]

Fig. 1(b) XRD pattern of the $ZnCo_2O_4$ sample. The diffraction peaks at 2θ = 19.3°, 31.7°, 36.8°, 38.5°, 44.9°, 55.7°, 59.5°, 65.4°, 74.1°, and 77.4° were indexed to the (111), (220), (311), (222), (400), (422), (511), (440), (620), and (533) planes of cubic spinel $ZnCo_2O_4$.[19,20] Furthermore, no additional peaks confirm the purity of the synthesized materials.

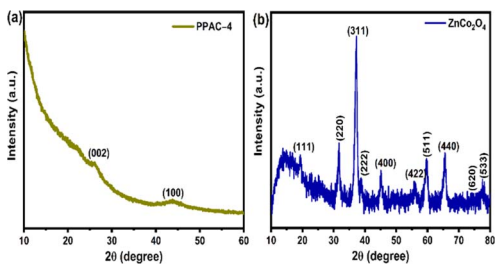

Fig. 1 XRD patterns of (a) PPAC-4 and (b) $ZnCo_2O_4$ samples.

N_2 adsorption/desorption studies

The N_2 adsorption/desorption isotherms of the PPAC-*N* samples shown in Fig. 2(a) and S2(a)† can be classified as type IV isotherms according to the IUPAC classification.[2,34] The isotherms demonstrate a steep uptake tendency at low relative pressure ($P/P_0 < 0.4$), which specifies the presence of micropores in all the samples. All the samples display an H4 type hysteresis loop, indicating the hierarchical porous structure with the co-existence of micro and mesopores in the carbon structure. Furthermore, the presence of macropores is indicated by the increased tail at the relatively high pressure range between 0.95 and 1.0 (P/P_0) in all the samples.[35,36] From Table S1 (ESI),† the SSA and pore volume increased from 855 to 2089 m^2 g^{-1} and from 0.47 to 1.28 cm^3 g^{-1}, respectively, as the concentration of the activating agent $KHCO_3$ increased from 1 M to 4 M. Further increasing the concentration (>4 M $KHCO_3$) resulted in a decrease in both the SSA and pore volume to 1530 m^2 g^{-1} and 0.97 cm^3 g^{-1}, respectively. According to these findings, an increase in the concentration of $KHCO_3$ from 1 to 4 M contributes to the formation of new pores as well as enlargement of existing ones, leading to an increase in the SSA and pore volume. However, we believe that higher $KHCO_3$ concentration (>4 M) leads to the structural contraction and collapse of the pores, thereby reducing the SSA and pore volume. The pore size distribution (PSD) curve shown in the inset of Fig. 2(a) and S2(b)† indicates the existence of mesopores with an average pore size of 3.9 nm and sizes ranging from 2 to 5 nm. From these results, it can be inferred that the PPAC-4 sample has a high SSA and pore volume, which can facilitate a significant accumulation of charge carriers and provide faster charge transport kinetics, thereby improving the supercapacitive performance of PPAC-4 in comparison to other activated carbons derived from pomelo peel.

The N_2 adsorption/desorption isotherms of $ZnCo_2O_4$ correspond to type-IV with H3 hysteresis loop [Fig. 2(b)], indicating the formation of a mesoporous structure.[19] The $ZnCo_2O_4$ sample displays an SSA of 46 m^2 g^{-1}, pore volume of 0.30 cm^3 g^{-1} and the sample mainly consists of mesopores with the pore

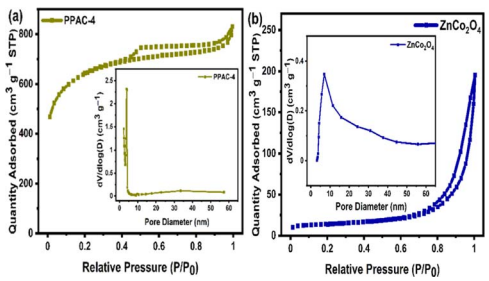

Fig. 2 N_2 adsorption/desorption isotherms, with the inset showing the pore size distribution plot of the (a) PPAC-4 and (b) $ZnCo_2O_4$ samples.

size mainly distributed between 5 and 30 nm, as indicated in the inset of Fig. 2(b) with an average pore size of 23.2 nm. The presence of mesopores in the as-prepared $ZnCo_2O_4$ often improves the interfacial electrode/electrolyte contact, accelerates the electrolyte ion diffusion and hence, superior pseudocapacitive performance can be achieved.[19,24]

Raman studies

Fig. 3(a) and S3(a) [ESI†] presents the Raman spectra of all the pomelo peel-derived activated carbon (PPAC-*N*) samples. The as-prepared PPAC-*N* samples possess two strong peaks centered at 1340 ± 5 cm^{-1} and 1580 ± 5 cm^{-1}, attributed to D bands (ascribed to the disordered carbon atoms) and G bands (attributed to the sp^2-hybridized graphitic carbon atoms), respectively.[37] The Raman spectra of PPAC-*N* samples are further deconvoluted into four distinct peaks, as indicated in Fig. 3(b) and S3(b–e).† According to the literature, the peaks centered at about 1250, 1342, 1495, and 1580 cm^{-1} correspond to D4-band, D1-band, D3-band and G-band, respectively. In general, the D4-band corresponds to the polyene/oligomer, the D1-band arises from the disorder/defects in the lattice structure of the carbon materials, the D3-band represents the amorphous carbon and the G-band is attributed to the sp^2 hybridized graphitic carbons embedded in the porous carbon framework.[2,38,39] The intensity ratio of the D1 and G band (I_{D1}/I_G) specifies the degree of graphitization of carbon materials.[38] The calculated I_{D1}/I_G ratios of the as-prepared samples are in the order PPAC-4 (0.54) < PPAC-3 (0.58) < PPAC-2 (0.75) < PPAC-5 (0.83) < PPAC-1 (0.94), respectively. The PPAC-4 sample exhibited lowest I_{D1}/I_G value, which corresponds to the highest degree of graphitization among all the pomelo peel-derived activated carbons. From the Raman and N_2 sorption analysis, it can be inferred that the PPAC-4 sample possesses a higher graphitization degree and high SSA, where the high SSA provides copious surface-active sites for the electrolyte ions to access, whereas the higher graphitization degree enhances the charge transport kinetics and promotes the penetration of electrolyte ions deep into the carbon framework. Hence, the optimized PPAC-4 sample was utilized for electrochemical experiments because of its excellent textural characteristics compared to the other pomelo peel-derived activated carbons.

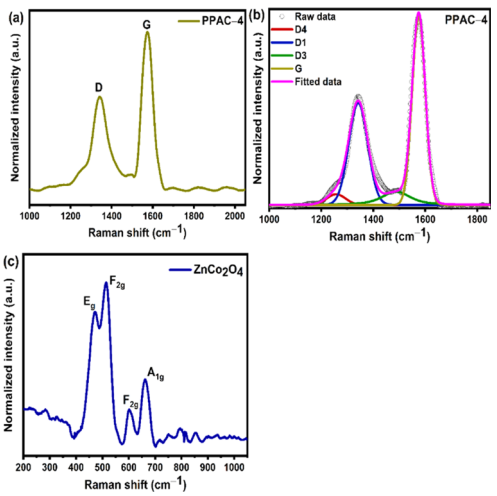

Fig. 3 (a) Raman spectra of the PPAC-4 sample. (b) Deconvoluted Raman spectra of the PPAC-4 sample. (c) Raman spectra of the $ZnCo_2O_4$ sample.

For the $ZnCo_2O_4$ sample, Raman peaks were observed at 471, 513, 602, and 665 cm^{-1}, which correspond to the E_g, $F_{2g}^{(2)}$, $F_{2g}^{(1)}$, and A_{1g} modes, respectively, as shown in Fig. 3(c). The Raman E_g mode at 471 cm^{-1} is ascribed to the strong stretching vibrations of Co–O and Zn–O bonds in the as-prepared $ZnCo_2O_4$ sample. On the other hand, the $F_{2g}^{(2)}$, $F_{2g}^{(1)}$, and A_{1g} modes at higher wavenumbers are attributed to the stretching vibration of the Co–O bond. Except for a slight shift in the peak position for a few peaks, all the peaks defined here indicate the formation of $ZnCo_2O_4$, which are in accordance with the previous reports.[19,23]

XPS analysis

The binding energy states of the PPAC-*N* and $ZnCo_2O_4$ samples analysed using XPS and the corresponding spectra are displayed in Fig. 4 and S4.† From the complete survey scan of the PPAC-*N* samples indicated in Fig. 4(a) and S4(a),† the peaks observed in the pomelo peel-derived activated carbons confirm the existence of carbon (C), oxygen (O) and nitrogen (N) in the survey spectrum, where these N and O groups are adsorbed on the surface of the porous carbon framework. The high-resolution C 1s, N 1s, and O 1s spectra of all the carbon samples are further deconvoluted into discrete peaks, as indicated in Fig. 4 (b–d) and S4(b–d)† to provide a deeper knowledge of individual elements in the as-prepared PPAC-*N* samples. The high-resolution C 1s spectra given in Fig. 4(b) and S4(b)† are split into three distinct peaks at 284.5 eV (C=C/C–C), related to the presence of graphitic carbon, 286.2 eV, belonging to C–O/C–N bonds, and 289.2 eV, related to the C=O bonds.[40,41] On the other hand, the nitrogen (N 1s) present in the as-prepared carbon samples are split into three peaks with energy of about 398.2 eV, 400 eV, and 402.3 eV [indicated in Fig. 4(c) and S4(c)†], which correspond to the pyridinic-N, pyrrolic-N, and quaternary-N, respectively.[40,41] Moreover, the high-resolution O 1s spectra given in Fig. 4(d) and S4(d)† are divided into two peaks at 531.6 (C=O) and 533.4 (C–O) eV.[2,41] According to the literature, the pyrrolic-N groups can engage in the faradaic reactions, generating additional pseudocapacitance, whereas quaternary-N bonds along with the oxygen functionalities effectively increase the wettability of the electrode material by the electrolyte.[42,43]

Fig. 4(e–h) demonstrates the composition and surface valence states of the as-prepared $ZnCo_2O_4$ sample. The survey scan of the $ZnCO_2O_4$ sample is shown in Fig. 4(e), which reveals the existence of zinc (Zn), cobalt (Co), oxygen (O), and small amount of carbon (C) in the as-prepared binary metal oxide sample. The high-resolution Zn 2p spectra in Fig. 4(f) consists of two prominent peaks at 1020 eV and 1043 eV, which are assigned to the Zn $2p_{3/2}$ and Zn $2p_{1/2}$ spin orbital states, demonstrating the Zn^{2+} oxidation state in the $ZnCo_2O_4$ sample. The Co 2p core level spectrum in Fig. 4(g) consists of two major

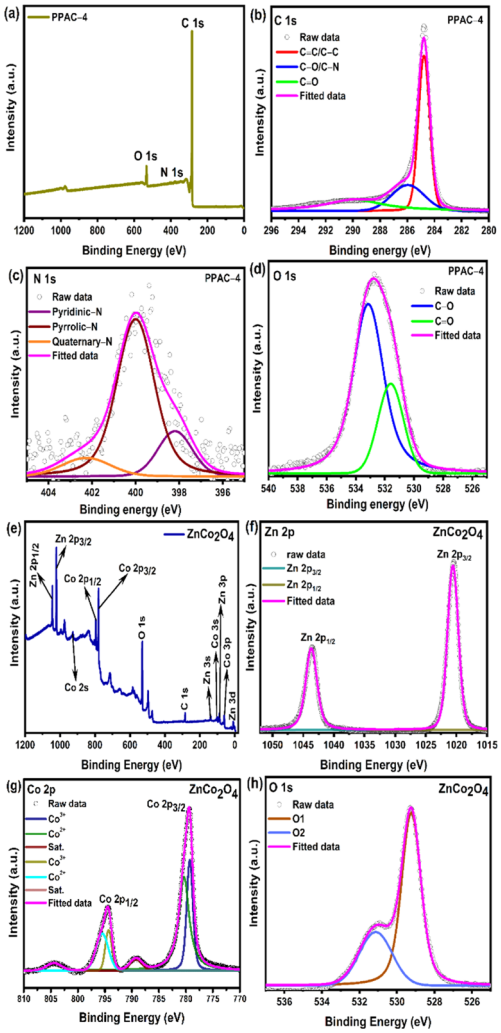

Fig. 4 XPS (a) full survey spectra of the PPAC-4 sample; high-resolution spectra of (b) C 1s, (c) N 1s and (d) O 1s peaks of the PPAC-4 sample. (e) Full survey spectra of $ZnCo_2O_4$ sample; high resolution spectra of the (f) Zn 2p, (g) Co 2p and (h) O 1s peaks of the $ZnCo_2O_4$ sample.

peaks with a peak spacing of ~15 eV centered at about 779 eV (Co $2p_{3/2}$) and 794 (Co $2p_{1/2}$) eV, indicating the formation of Co^{3+} species in the $ZnCo_2O_4$ sample. Following peak deconvolution, the Co^{3+} oxidation state in $ZnCo_2O_4$ was identified by two peaks at binding energies of 779.1 and 794.3 eV, and its Co^{2+} oxidation state by two more peaks at 780.4 and 795.6 eV. Additionally, the broad peaks at 788.5 eV and 802.4 eV are called the satellite peaks and they provide additional evidence that the sample possess the Co^{2+} oxidation state. The core level spectra of O 1s is deconvoluted into two peaks (as shown in Fig. 4(h)) centered at 529.2 (O 1) and 531.2 (O 2) eV. These O1 and O2 peaks represent the metal–oxygen bonds and the absorbed –OH molecules on the surface of the $ZnCo_2O_4$ sample, respectively.[19,23,25] Based on the above analysis, we can deduce that Zn^{2+} and Co^{2+}/Co^{3+} co-exist in $ZnCo_2O_4$, which is in line with the results that have been previously published. The elemental composition (*i.e.*, the relative concentration of Zn, Co, O, and C present in the samples) was calculated from the core energy levels of the individual elements using the peak areas.[44] The percentages of Zn, Co, O, and C were 13.7%, 31.2%, 51.3%, and 2.8%, respectively.

Morphological analysis

As indicated in Fig. 5(a and b), the field emission scanning electron microscopy (FESEM) images of the PPAC-4 sample reveal the presence of a hierarchical porous morphology containing disordered/uneven carbon structures with interconnected layered networks. These interconnected networks are particularly beneficial for the smooth and rapid transport of the electrolyte ions inside the porous carbon matrix and also helps in the complete utilization of the carbon surface during the electrochemical charge discharge process. Porous carbon along with the interconnected layered network are further confirmed with the HAADF-STEM imaging of the PPAC-4 sample shown in Fig. 5(c). The porous structure is beneficial for the accumulation of charge carriers whereas the interconnected layered network facilitates the faster transport of the ions and fully exposes the porous carbon matrix to the electrolyte ions. The energy-dispersive X-ray spectroscopy (EDX) elemental maps of the PPAC-4 sample [shown in Fig. 5(d–f)] obviously show the existence of C, N, and O elements, where the oxygen and nitrogen elements are randomly distributed on the surface of the porous carbon framework.

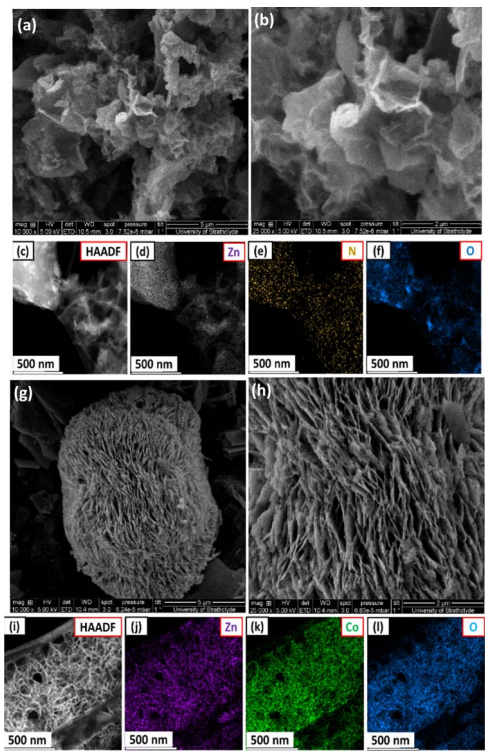

Fig. 5 (a and b) FESEM morphologies of the PPAC-4 sample at different magnifications. (c) HAADF image and (d–f) EDX elemental (C, N, and O) maps of the PPAC-4 sample. (g and h) FESEM morphologies of the $ZnCo_2O_4$ sample at different magnifications. (i) HAADF image and (j–l) EDX elemental (Zn, Co, and O) maps of the $ZnCo_2O_4$ sample.

The FESEM images of the $ZnCo_2O_4$ sample shown in Fig. 5(g) display the presence of spherical structures. A closer look at the FESEM image (Fig. 5(h)) reveals that the spherical $ZnCo_2O_4$ architectures are made up of several tightly interconnected porous nanosheets, which assembled to form microspheres. Notably, these nanosheets are in contact with one another, which may improve the mechanical strength and produce necessary openings for the rapid diffusion of electrolyte ions during the redox electrochemical activity, which is extremely useful for improving the electrochemical performance.[19] The HAADF-STEM image of the $ZnCo_2O_4$ sample (shown in Fig. 5(i)) further confirms the existence of interconnected nanosheets. The elemental maps of the sheet like $ZnCo_2O_4$ microspheres are shown in Fig. 5(j–l), revealing the uniformly distributed O, Co, and Zn in the $ZnCo_2O_4$ sample.

Electrochemical performance of PPAC-4 and $ZnCo_2O_4$ electrodes measured in 2 M KOH electrolyte

The electrochemical performance of PPAC-4 and $ZnCo_2O_4$ electrodes were investigated in detail in the three-electrode configuration employing CV, GCD, and EIS techniques with 2 M KOH electrolyte. Fig. 6(a) and (c) show the electrochemical performance of PPAC-4 and $ZnCo_2O_4$ electrodes, which was examined across negative (−1 to 0 V) and positive (0 to 0.6 V) potential windows. Fig. 6(a) displays the PPAC-4 electrode's CV findings at various scan rates. The CV plot shows a quasi-rectangular shape with no redox peak, indicating the purity of the as-synthesized PPAC-4 electrode. This validates the characteristic EDLC nature of the PPAC-4 material. Similarly, the GCD plots in Fig. 6(b) yield a linear charge/discharge curve, confirming the double layer charge storage mechanism of the as-prepared carbon material. The CV measurements for the $ZnCO_2O_4$ sheet-like microspheres are performed between 5 and 100 mV s^{-1} scan rate within 0 to 0.6 V, as shown in Fig. 6(c). The form of the CV curves illustrated in Fig. 6(c) indicates that the $ZnCO_2O_4$ electrode has pseudocapacitive charge storage properties. The CV curves shown in Fig. 6(c) present a pair of redox reaction peak indicating the faradaic redox reactions, which might be related to the Co–O/Co–O–OH functional groups of $ZnCO_2O_4$.[19,23] The redox current response rises as the scan rate increases from 5 to 100 mV s^{-1}, suggesting that the sheet-like $ZnCo_2O_4$ microspheres have a quick redox reaction, strong electron conductivity, and rate capacity. Additionally, when the scan rate increases, the anodic and cathodic peaks move toward higher and lower potentials, respectively. This phenomenon may be related to the quasi-reversible nature of the anodic peaks and enhanced polarization at high scan rates.[20,23] Fig. 6(d) displays the GCD plot of the $ZnCo_2O_4$ electrode. The nonlinear charge discharge curves at various current densities within the 0 to 0.6 V potential window further indicates the redox reactions in the electrode material and is in agreement with the CV curves shown in Fig. 6(c). Fig. 6(e) shows the effect of current density on the specific capacitance for both PPAC-4 and $ZnCo_2O_4$ electrodes. The $ZnCo_2O_4$ electrode showed a specific capacitance of 422 F g^{-1} at 1 A g^{-1} (specific capacity of 253 C g^{-1} at 1 A g^{-1} current density), which decreased to 328 F g^{-1} at 30 A g^{-1} current density, thus retaining ~78% of its starting capacitance. In the case of the PPAC-4 electrode, the specific capacitance was found to be 356 F g^{-1} at 1 A g^{-1}. Furthermore, the PPAC-4 electrode retained ~70% of its capacitance at 30 A g^{-1} current density. High specific capacitances are obtained at low current densities, which indicates higher interaction between the electrode and electrolyte ions. As the current density increases, the capacitance steadily decreases, which is most likely caused by the low diffusion of electrolyte ions (owing to less reaction time) or less number of active sites participating in redox processes at high current densities. The performance of the PPAC-4 and

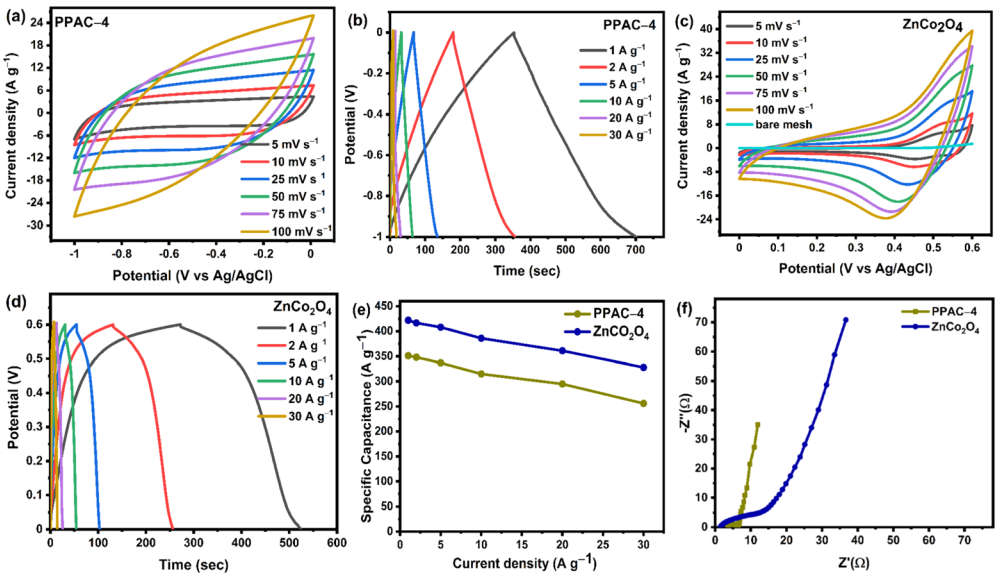

Fig. 6 (a) CV curves of the PPAC-4 electrode at different scan rates. (b) GCD curves of the PPAC-4 electrode at various current densities. (c) CV curves of the $ZnCo_2O_4$ electrode at different scan rates. (d) GCD curves of the $ZnCo_2O_4$ electrode at various current densities. (e) The specific capacitance *versus* current density for the PPAC-4 and $ZnCo_2O_4$ electrodes. (f) Nyquist plots of the PPAC-4 and $ZnCo_2O_4$ electrodes.

$ZnCo_2O_4$ electrodes was further investigated using EIS, and the corresponding Nyquist curve and equivalent circuit model are displayed in Fig. 6(f), S5a and b,† respectively. In the low frequency area, the PPAC-4 electrode exhibits a nearly vertical line, indicating almost ideal capacitive behaviour. In the high frequency zone, a semi-circle reveals the charge transfer resistance (R_{ct}). In the same low frequency range, the $ZnCo_2O_4$ electrode shows a more slanted curve, which suggests that pseudocapacitance is mostly responsible. After fitting the equivalent circuit model, the R_{ct} of PPAC-4 (2.62 Ω) was found to be less than that of the $ZnCo_2O_4$ (14.4 Ω) electrode. This is because $ZnCo_2O_4$ charge transfer includes slower redox processes than the simple surface adsorption/desorption that occurs in the PPAC-4 electrode. This is because of the presence of heteroatoms present in the PPAC-4 sample, which accelerates the charge transport kinetics inside the carbon matrix. The length of the Warburg line, or the slope of the 45° section in the mid frequency range, is particularly useful in expressing the ion diffusion process.[45] Since, the Warburg line of PPAC-4 is much shorter than that of $ZnCo_2O_4$, rapid ionic diffusion takes place in the porous interconnected carbon framework. The equivalent circuit model of PPAC-4 and $ZnCo_2O_4$ electrodes circuits is shown in Fig. S6(a and b) [ESI].† The components that make up the circuit model are Warburg impedance (W), constant phase element (Q), double-layer capacitance (C_{dl}), R_s, and R_{ct}. The ion transfer occurring inside the pores of the electrode is represented by the R_{ct}–C_{dl} circuit. The inclined line seen in the low-frequency area of the Nyquist plots illustrates the capacitive behaviour of the electrode denoted by Q in the equivalent circuit. From these findings, it can be concluded that the PPAC-4 electrode typically displays a EDLC mechanism whereas the $ZnCo_2O_4$ electrode stores the charge *via* the faradaic redox reactions.

Electrochemical performance of the asymmetric supercapacitor

The applicability of $ZnCo_2O_4$ and PPAC-4 was estimated using an asymmetric Swagelok supercapacitor cell with $ZnCo_2O_4$ as the positive electrode and PPAC-4 as the negative electrode with HEC–KOH biopolymer gel film as the electrolyte. The CV curves depicted in Fig. 7(a) indicate the capacitance involvement from both the electric double layer mechanism and pseudocapacitance mechanism at each scan rate. Moreover, significant redox peaks are visible even at high scan rates due to the strong pseudocapacitive nature of the $ZnCo_2O_4$ electrode. The shape of the CV curves remained stable even at 100 mV s^{-1} scan rate, demonstrating the remarkable reversibility and rate capability of the supercapacitor. The GCD profiles of the $ZnCo_2O_4$//PPAC-4 supercapacitor at various current densities are displayed in Fig. 7(b). On the basis of the GCD curves, the specific capacitance of the device attained at 1 A g^{-1} was 84 F g^{-1}, which reduced to 41 F g^{-1} at 30 A g^{-1}. The drop in the specific capacitance at increased current density could be attributed to the limited ability of the ions to penetrate into the active material, resulting in a loss in specific capacitance. The prominent performance of this asymmetric supercapacitor can be

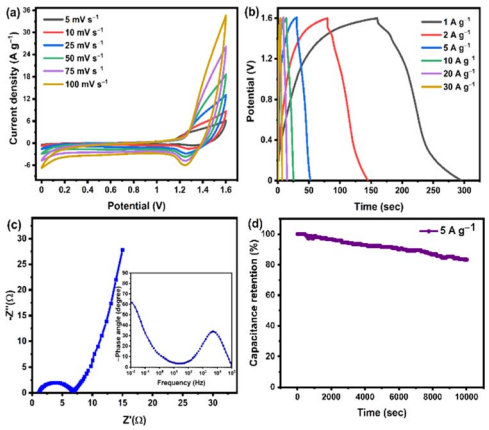

Fig. 7 (a) CV curves at different scan rates. (b) GCD curves at different current densities. (c) EIS plot with an equivalent circuit. (d) Long-term cycling stability tests of the $ZnCo_2O_4$//PPAC-4 asymmetric supercapacitor for 10 000 cycles performed at a current density of 5 A g^{-1}.

related to the combined effect between $ZnCo_2O_4$ microspheres and PPAC-4, where the high SSA of PPAC-4 provides bulk surface-active sites for the ions to access, while $ZnCo_2O_4$ provides high specific capacitance. To determine the resistance given by the asymmetric supercapacitor, EIS was performed, and the related Nyquist plot is presented in Fig. 7(c). The device exhibited a low series resistance of 1.15 Ω, which includes the resistance from the electrode, gel electrolyte film, and electrode/electrolyte interface.[46] The charge transfer resistance was observed to be 5.68 Ω, which is the resistance offered by electrode materials. The steep slope in the lower frequency area of the Nyquist plot may be attributed to the Warburg behaviour, which results from the fast diffusion of electrolyte ions across the electrode/electrolyte interface. The inset of Fig. 7(c) shows the Bode plot of phase angle plotted against frequency for the fabricated asymmetric device. The phase angle of −61.6° at low frequency is indicative of both pseudocapacitance and double layer capacitance contribution. The Nyquist plot of asymmetric supercapacitor was fitted with the equivalent circuit model to analyze the mechanism of the charge transfer process. Fig. S7(a) [ESI†] shows the equivalent circuit used for fitting and the first resistance represents the series resistance (R_s). The parallel combination of capacitance and resistance (Q, R_{ct}) in the first part indicates the formation of double layer and the second part (Q) represents the diffusion region. The final part (Z_W) represents the Warburg diffusion. Furthermore, the cyclic performance of the as-prepared asymmetric supercapacitor was examined by the repetitive charge/discharge measurements for 10 000 cycles. The $ZnCo_2O_4$//PPAC-4 asymmetric supercapacitor has a remarkable cyclic stability of 83% capacitance retention over 10 000 cycles at 5 A g^{-1}, as indicated in Fig. 7(d). Such a superior performance is mainly related to the pseudocapacitive nature of sheet-like $ZnCo_2O_4$ microspheres and large SSA (2089 m^2 g^{-1}) of PPAC-4, which facilitates quick ion transfer and bulk active sites for charge storage.

To evaluate the feasibility of the $ZnCo_2O_4$//PPAC-4 asymmetric supercapacitor for practical applications, the Ragone

plot based on the GCD curves is plotted and compared with the existing literature in Table 1 as well as in Fig. 8(a). The as-prepared asymmetric supercapacitor achieved a maximum energy density of 29.8 W h kg^{-1} at a power density of 796.3 W kg^{-1}, and the energy density was reduced to 14.5 W h kg^{-1} at a higher power density of 23.8 kW kg^{-1}. This electrochemical performance of our $ZnCo_2O_4$//PPAC-4 asymmetric supercapacitor with bio-polymer gel electrolyte film outperforms many previously reported asymmetric devices with aqueous electrolytes, as indicated in Table 1.[7,23,47–53] We believe the synergistic effect of the high SSA activated carbon (PPAC-4) and sheet-like $ZnCo_2O_4$ microspheres, where PPAC-4 provides rich active sites for charge storage and $ZnCo_2O_4$ provides abundant channels for electrolyte ion transfer with rich pseudocapacitance to the asymmetric device. However, the performance of our bio-polymer gel electrolyte film-based asymmetric supercapacitor is still lower than some of the aqueous electrolyte-based devices, for example, $ZnCo_2O_4$ quasi cubes//AC (34.4 W h kg^{-1} at 860.1 W kg^{-1})[23] and $NiCo_2O_4$-HLPBC//AC (30.7 W h kg^{-1} at 900 W kg^{-1}).[49] The realistic feasibility of the $ZnCo_2O_4$//PPAC-4 asymmetric supercapacitor for practical applications was studied by connecting it to a small motor/fan. Fig. 8(b) shows the asymmetric device charged to 1.6 V using a power supply. After charging for 1 minute, the device terminals are connected to motor as the load. As shown in Fig. 8(c), the as-prepared asymmetric device is able to power up the motor (for more than 4 minutes, see the corresponding video in ESI†), demonstrating the profound performance of the device for practical applicability in energy storage applications.

Table 1 Energy density and power density of the $ZnCo_2O_4$//PPAC-4 compared with other asymmetric supercapacitors reported in the literature

Device	Energy density (W h kg^{-1})	Power density (W kg^{-1})	Ref.
$ZnCo_2O_4$//AC	20.3	855	48
$ZnCo_2O_4$//AC	27.7	158.5	52
$NiCo_2S_4$-RSAC//RSAC	24.5	700	50
$ZnCo_2O_4$//AC	26.2	716	47
$NiCo_2O_4$-CSPC//CSPC	23.9	1298	53
$CoMn_3O_8$//HBFC	24.3	850	7
$ZnCo_2O_4$//$ZnCo_2O_4$	11.8	2504	51
$ZnCo_2O_4$//AC	34.4	860.1	23
$NiCo_2O_4$-HLPBC//AC	30.7	900	49
$ZnCo_2O_4$//PPAC-4	29.8	796.3	This work

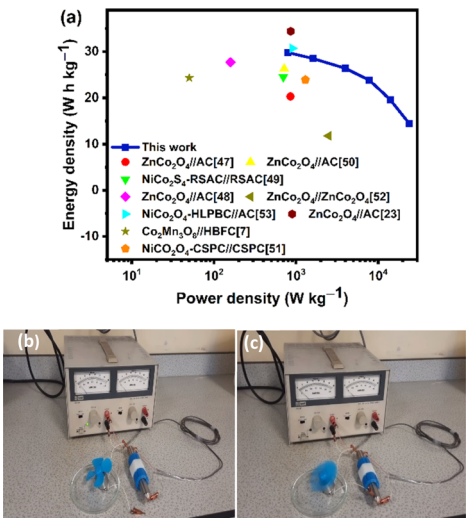

Fig. 8 (a) Ragone plot of the $ZnCo_2O_4$//PPAC-4 asymmetric supercapacitor compared with other reported binary metal oxide//activated carbon asymmetric supercapacitor devices reported in the literature; practical application of the $ZnCo_2O_4$//PPAC-4 asymmetric supercapacitor. (b) Device being charged at 1.6 V with power supply. (c) Performance of a motor/fan connected to the asymmetric supercapacitor.

Conclusion

In summary, asymmetric supercapacitors fabricated from pomelo peel waste-derived activated carbon (PPAC-4) and $ZnCo_2O_4$ nanostructures show great potential for developing sophisticated energy storage devices. Morphological analysis using SEM and TEM analyses show that PPAC-4 has disordered/uneven carbon structures with interconnected layered networks, while $ZnCo_2O_4$ reveals spherical structures with tightly interconnected nanosheets. In addition, the as-prepared sheet-like $ZnCo_2O_4$ microspheres as the positive electrode exhibit a high specific capacitance of 422 F g^{-1} at 1 A g^{-1} current density, whereas the specific capacitance of PPAC-4 is 356 F g^{-1} at 0.5 A g^{-1} in the three-electrode configuration. Furthermore, the fabricated $ZnCo_2O_4$//PPAC-4 asymmetric supercapacitor with bio-polymer gel electrolyte displayed excellent electrochemical performance with superior energy density of 29.8 W h kg^{-1} at a power density of 796.3 W kg^{-1}. Also, the fabricated device retained 83% of its performance even after 10 000 repetitive cycles at 5 A g^{-1} current density. This work not only extends the application of pomelo peel waste to the electrochemical energy storage application (high value-added activated carbon as negative electrodes) but also demonstrates that $ZnCo_2O_4$ and PPAC-4 are suitable for an affordable, high-performance battery-type supercapacitor to meet the high power and energy needs.

Author contributions

RKKR designed, carried out and analysed the majority of the practical work, as well as written the manuscript draft. LŠ performed the XPS measurements and helped with data fitting. AI conceptualized, actively supervised and assisted in interpreting the results. AI and LŠ provided inputs to the manuscript.

Conflicts of interest

There are no conflicts to declare.

Acknowledgements

AI gratefully acknowledges Scottish Funding Council (SFC) Global Challenges Research Fund (GCRF) and Strathclyde

Centre for Doctoral Training (SCDT), Centre for Interdisciplinary Sustainable Practices of Research in Energy (C-INSPRE), for co-funding Kiran's studentship and this project. She also gratefully acknowledges UK Research and Innovation (UKRI), Engineering and Physical Sciences Research Council (EPSRC) for the Fellowship grant (EP/P011500/1). LŠ would like to thank Engineering and Physical Sciences Research Council (EPSRC) UK, for NEXUS facility at Newcastle University (NS/A000015/1). The authors would like to thank Dr Andrew Callander for his assistance in Raman Measurements, Dr Paul Edwards for FESEM measurements, and Aaron Naden for HRTEM measurements.

References

1 O. P. Nanda, A. G. Prince, L. Durai and S. Badhulika, *Energy Fuels*, 2023, **37**, 4701–4710.
2 K. K. R. Reddygunta, A. Callander, L. Šiller, K. Faulds, L. Berlouis and A. Ivaturi, *Int. J. Energy Res.*, 2022, **46**, 16512–16537.
3 T. Jiang, Y. Wang and G. Z. Chen, *Small Methods*, 2023, 2201724.
4 P. Makkar, A. Malik and N. N. Ghosh, *ACS Appl. Energy Mater.*, 2021, **4**, 6015–6024.
5 K. Yousefipour, R. Sarraf-Mamoory and A. C. Maleki, *J. Energy Storage*, 2023, **59**, 106438.
6 S. Alam, F. Fiaz, M. I. Khan, M. Z. Iqbal and H. H. Hegazy, *J. Alloys Compd.*, 2023, 171007.
7 H. A. Hamouda, S. Cui, X. Dai, X. Xie, H. Peng, G. Ma and Z. Lei, *J. Energy Storage*, 2022, **47**, 103616.
8 G. S. Dos Reis, S. H. Larsson, H. P. de Oliveira, M. Thyrel and E. Claudio Lima, *Nanomaterials*, 2020, **10**, 1398.
9 Q. Liang, L. Ye, Z.-H. Huang, Q. Xu, Y. Bai, F. Kang and Q.-H. Yang, *Nanoscale*, 2014, **6**, 13831–13837.
10 C. Peng, J. Lang, S. Xu and X. Wang, *RSC Adv.*, 2014, **4**, 54662–54667.
11 Z. Wang, Y. Tan, Y. Yang, X. Zhao, Y. Liu, L. Niu, B. Tichnell, L. Kong, L. Kang and Z. Liu, *J. Power Sources*, 2018, **378**, 499–510.
12 G. Qu, S. Jia, H. Wang, F. Cao, L. Li, C. Qing, D. Sun, B. Wang, Y. Tang and J. Wang, *ACS Appl. Mater. Interfaces*, 2016, **8**, 20822–20830.
13 L. Fang, F. Wang, T. Zhai, Y. Qiu, M. Lan, K. Huang and Q. Jing, *Electrochim. Acta*, 2018, **259**, 552–558.
14 X. Yu, B. Lu and Z. Xu, *Adv. Mater.*, 2014, **26**, 1044–1051.
15 R. BoopathiRaja, M. Parthibavarman and A. N. Begum, *Vacuum*, 2019, **165**, 96–104.
16 J. Sun, C. Xu and H. Chen, *J. Materiomics*, 2021, **7**, 98–126.
17 N. Zhao, H. Fan, M. Zhang, J. Ma, W. Zhang, C. Wang, H. Li, X. Jiang and X. Cao, *Electrochim. Acta*, 2019, **321**, 134681.
18 J. Pu, J. Wang, X. Jin, F. Cui, E. Sheng and Z. Wang, *Electrochim. Acta*, 2013, **106**, 226–234.
19 H. Chen, J. Wang, X. Han, F. Liao, Y. Zhang, L. Gao and C. Xu, *Ceram. Int.*, 2019, **45**, 8577–8584.
20 J. A. Rajesh, B.-K. Min, J.-H. Kim, S.-H. Kang, H. Kim and K.-S. Ahn, *J. Electroanal. Chem.*, 2017, **785**, 48–57.
21 Y. Zhang, L. Li, H. Su, W. Huang and X. Dong, *J. Mater. Chem. A*, 2015, **3**, 43–59.
22 Y. Ma, X. Xie, W. Yang, Z. Yu, X. Sun, Y. Zhang, X. Yang, H. Kimura, C. Hou and Z. Guo, *Adv. Compos. Hybrid Mater.*, 2021, 1–19.
23 H. Chen, X. Du, J. Sun, H. Mao, R. Wu and C. Xu, *Appl. Surf. Sci.*, 2020, **515**, 146008.
24 J. Zhu, D. Song, T. Pu, J. Li, B. Huang, W. Wang, C. Zhao, L. Xie and L. Chen, *Chem. Eng. J.*, 2018, **336**, 679–689.
25 A. J. C. Mary and A. C. Bose, *Appl. Surf. Sci.*, 2017, **425**, 201–211.
26 F. Wang, J. Ma, K. Zhou and X. Li, *Mater. Chem. Phys.*, 2020, **244**, 122215.
27 S. Kumar and Y.-P. Fu, *Sustainable Energy Fuels*, 2021, **5**, 3987–4001.
28 A. Siddiqa, D. Sushmitha, K. Nagaraja, D. Nagaraju and M. Padaki, *J. Electron. Mater.*, 2023, **52**, 1717–1729.
29 A. Siddiqa, N. DH and M. Padaki, *Energy Fuels*, 2022, **36**, 13286–13295.
30 H. Wang, G. Ma, Y. Tong and Z. Yang, *Ionics*, 2018, **24**, 3123–3131.
31 J. Bai, S. Mao, F. Guo, R. Shu, S. Liu, K. Dong, Y. Yu and L. Qian, *New J. Chem.*, 2022, **46**, 10752–10764.
32 H. Li, Z. Sun, L. Zhang, Y. Tian, G. Cui and S. Yan, *Colloids Surf., A*, 2016, **489**, 191–199.
33 M. Sivachidambaram, J. J. Vijaya, L. J. Kennedy, R. Jothiramalingam, H. A. Al-Lohedan, M. A. Munusamy, E. Elanthamilan and J. P. Merlin, *New J. Chem.*, 2017, **41**, 3939–3949.
34 J. Liu, H. Li, H. Zhang, Q. Liu, R. Li, B. Li and J. Wang, *J. Solid State Chem.*, 2018, **257**, 64–71.
35 D. Jain, J. Kanungo and S. Tripathi, *J. Alloys Compd.*, 2020, **832**, 154956.
36 F. Ran, X. Yang, X. Xu, S. Li, Y. Liu and L. Shao, *Chem. Eng. J.*, 2021, **412**, 128673.
37 Y. Lin, Z. Chen, C. Yu and W. Zhong, *ACS Sustain. Chem. Eng.*, 2019, **7**, 3389–3403.
38 D. Zhang, B. Yang, W. She, S. Gao, J. Wang, Y. Wang, K. Wang, H. Li and L. Han, *J. Power Sources*, 2021, **506**, 230103.
39 Y. Wang, B. Yang, D. Zhang, H. Shi, M. Lei, H. Li and K. Wang, *Appl. Surf. Sci.*, 2020, **512**, 145711.
40 X. Wu, Z. Tian, L. Hu, S. Huang and J. Cai, *RSC Adv.*, 2017, **7**, 32795–32805.
41 L. Shi, L. Jin, Z. Meng, Y. Sun, C. Li and Y. Shen, *RSC Adv.*, 2018, **8**, 39937–39947.
42 C. Chen, D. Yu, G. Zhao, B. Du, W. Tang, L. Sun, Y. Sun, F. Besenbacher and M. Yu, *Nano Energy*, 2016, **27**, 377–389.
43 D. Puthusseri, V. Aravindan, S. Madhavi and S. Ogale, *Energy Environ. Sci.*, 2014, **7**, 728–735.
44 A. G. Shard, *J. Vac. Sci. Technol., A*, 2020, **38**, 041201.
45 Y. Li, N. Yu, P. Yan, Y. Li, X. Zhou, S. Chen, G. Wang, T. Wei and Z. Fan, *J. Power Sources*, 2015, **300**, 309–317.
46 M. A. A. Mohd Abdah, N. H. N. Azman, S. Kulandaivalu and Y. Sulaiman, *Sci. Rep.*, 2019, **9**, 16782.
47 J. Bhagwan, S. K. Hussain and J. S. Yu, *J. Alloys Compd.*, 2020, **815**, 152456.

48 L. Chen, Y. Jiao, Z. Li and Y. Gao, *Electrochim. Acta*, 2019, **299**, 388–394.
49 D. Guo, L. Zhang, X. Song, L. Tan, H. Ma, J. Jiao, D. Zhu and F. Li, *New J. Chem.*, 2018, **42**, 8478–8484.
50 R. Jiang, C. Zhou, Y. Yang, S. Zhu, S. Li, J. Zhou, W. Li and L. Ding, *Diamond Relat. Mater.*, 2023, 110322.
51 J. A. Rajesh, B.-K. Min, J.-H. Kim, H. Kim and K.-S. Ahn, *J. Electrochem. Soc.*, 2016, **163**, A2418.
52 Y. Shang, T. Xie, C. Ma, L. Su, Y. Gai, J. Liu and L. Gong, *Electrochim. Acta*, 2018, **286**, 103–113.
53 R. Wang, X. Li, Z. Nie, Y. Wang, Y. Zhao and H. Wang, *Energy Fuels*, 2022, **36**, 13256–13265.